

Supplementary material

A. Latitudinal profiles of atmospheric conditions

5

Table S1 Latitudinal profiles of irradiation time, temperature and relative humidity (ERA5), and NO₂/BC ratio (CAM5) for the ARCTEx transport scenarios: summer low-altitude (SL), summer high-altitude (SH), winter low-altitude (WL), winter high-altitude (WH). Latitudinal profiles extracted in the region of interest between 40°N and 90°N, in the pressure range 1000-800 hPa (low-altitude) and 600-400 hPa (high-altitude), in July (summer) and January (Winter). 40-90°N transport corresponding to 5 experimental days in AIDA (10°N = 1 experimental day). Median calculated for equidistant latitude bands 10° wide.

10

Experiment day	1	2	3	4	5
Simulated latitude [°N]	40-50	50-60	60-70	70-80	80-90
Irradiation time [h]					
SL – SH	16	20	22	24	24
WL – WH	8	4	2	0	0
Temperature [°C]					
SL	21	15	11	3.0	0.0
SH	-35	-39	-40	-40	-41
WL	-9.0	-16	-21	-21	-21
WH	-52	-55	-57	-57	-58
Relative humidity [%]					
SL	55	69	68	78	83
SH	47	56	55	49	48
WL	63	78	86	85	85
WH	44	57	62	61	60
NO ₂ /BC ratio [-]					
SL	2.8	0.78	0.60	0.22	0.20
SH	4.2	2.4	1.6	1.5	1.39
WL	6.7	11	9.6	3.9	1.6
WH	8.2	10	12	10	7.5

15

Table S2 Daily mean of experimental conditions measured in the AIDA chamber for the ARCTEx transport scenarios: summer low-altitude (SL), summer high-altitude (SH), winter low-altitude (WL), winter high-altitude (WH). 40-90°N transport corresponding to 5 experimental days in AIDA (10°N = 1 experimental day). Median calculated for equidistant latitude bands 10° wide.

Experiment day	1	2	3	4	5
Simulated latitude [°N]	40-50	50-60	60-70	70-80	80-90
Irradiation time [h]					
SL – SH	16	20	22	24	24
WL -WH	8	4	2	0	0
Temperature, T [°C]					
SL	21	15	10	3	0.0
SH	-35	-40	-41	-41	-41
WL	-9.8	-16	-20	-21	-22
WH	-52	-56	-58	-59	-59
Relative humidity, RH [%]					
SL	44	62	65	77	79
SH	53	63	58	49	49
WL	57	72	75	74	71
WH	56	57	57	57	58
NO ₂ /BC ratio [-]					
SL	3.5	2.0	2.0	2.8	5.2
SH	2.8	1.7	1.0	1.3	1.6
WL	5.4	7.6	6.4	2.2	3.3
WH	5.7	6.8	12	8.2	7.5

20 **Table S3 Ratio between daily averaged AIDA conditions over latitudinally averaged ERA5 and CAMS data.**

Experiment day	1	2	3	4	5
Simulated Latitude [°N]	40-50	50-60	60-70	70-80	80-90
Measured/simulated ratio					
Temperature [-]					
SL	1.00	1.00	0.99	1.00	1.00
SH	1.00	0.99	0.99	0.99	0.99
WL	0.99	1.00	1.00	0.99	0.99
WH	0.99	0.99	0.99	0.99	0.99
Relative humidity [-]					
SL	0.80	0.90	0.96	1.00	0.95
SH	1.13	1.12	1.06	1.01	1.03
WL	0.90	0.93	0.89	0.87	0.85
WH	1.27	1.01	0.92	0.94	0.97
NO2/BC ratio [-]					
SL	1.25	2.53	3.37	12.87	26.10
SH	0.65	0.69	0.68	0.86	1.15
WL	0.81	0.66	0.67	0.55	2.13
WH	0.70	0.66	1.07	0.82	1.00

B. Characterization of fresh mini-CAST soot

25

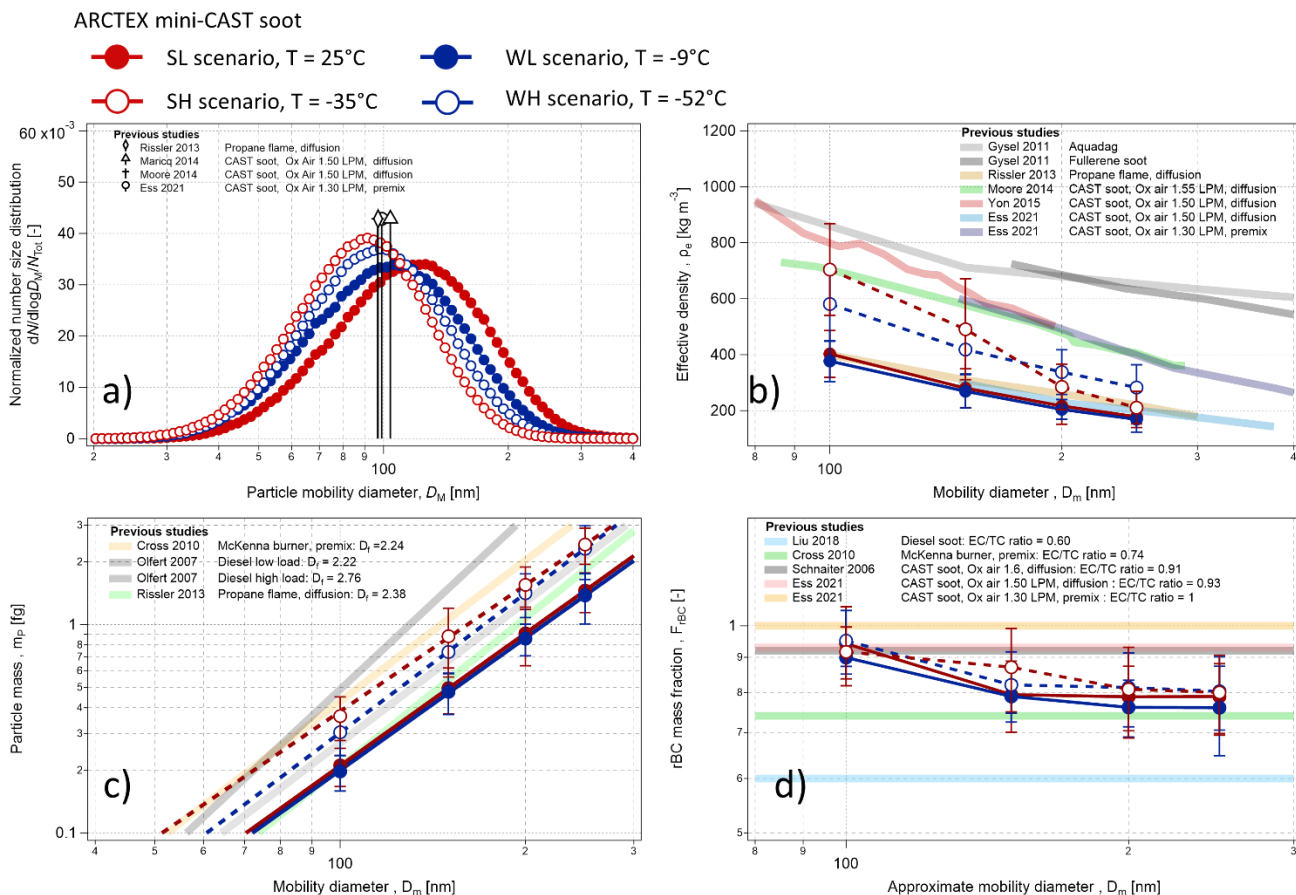
In this section, we describe the fundamental properties of fresh soot injected in the AIDA chamber, aged in dark conditions and in the absence of ozone and nitrogen dioxide for less than 60 minutes after the injection time (Table 1) under the 4 transport scenario conditions.

25 The number size distribution measured with the SMPS showed a non-negligible variability characterized
 30 by a minimum geometric mean diameter of 80 nm for SL to a maximum of 104 nm for SH, while the winter experiments shared a relatively similar size of around 92-93 nm (Figure S 1a). Although these values were similar to previous studies measuring soot produced with diffusion flame burners with slightly different oxidative air flows (Ess et al., 2021; Maricq, 2014; Moore et al., 2014; Rissler et al., 2013), we expected higher reproducibility of BC mobility diameter. The soot showed a clear decrease of
 35 effective density with particle diameter (Figure S 1b), as expected for fractal aggregates. During the low-altitude experiments, the density showed a common decrease of ρ_e from 400 kg m⁻³ at 100 nm to 200 kg m⁻³ at 250 nm, being in agreement with diffusion-flame soot (Ess et al., 2021; Rissler et al., 2013). However, these ARTCEX values were substantially lower compared to mini-CAST soot obtained under
 40 different combustion regimes (Ess et al., 2021; Moore et al., 2014; Yon et al., 2015) and to BC standards such as fullerene soot and acquadag (Gysel et al., 2011). Interestingly, the soot injected at colder temperatures (WH and SH) was denser, with ρ_e ranging from 590-770 kg m⁻³ at 100 nm to 220-380 kg m⁻³ at 250 nm.

45 Similar to density, the soot injected in AIDA showed lower fractal dimensions compared to previous studies (Figure S 1c). Low d_f values (2.01-2.21) indicated the production of complex aggregates, agreeing with the low effective density discussed above. As a matter of fact, diesel soot (Olfert et al., 2007), and diffusion (Rissler et al., 2013) or premix (Cross et al., 2010) soot was characterized by already more compact aggregates. The rBC mass fraction (F_{rBC}) was compared with EC/TC fractions observed in previous studies. The latter showed high variabilities connected with the type of fuel (diesel, EC/TC=0.6, Liu et al., 2018) and combustion conditions (diffusion and premixed flame; Ess et al., 2021). During all
 50 ARCTEx experiments, the fraction of rBC appeared to decrease with the particle diameter from a maximum of 95% to a minimum of 75%. This range fell between the premixed McKenna burner (Cross et al., 2010) and the diffusion mini-CAST burner with oxidativeoxidative air flows of 1.60-1.55 (Ess et al., 2021; Schnaiter et al., 2006). The comparison between F_{rBC} and EC/TC ratio must be treated with

55 caution, given the systematic differences observed between the mass concentration of rBC and EC (Pileci et al., 2021).

Despite the slightly higher density and lower fractal dimension, the soot particles produced during ARCTEx appeared to be representative of soot generated with various diffusion burners operated at similar flow rates of propane and oxidative air. It is interesting to note that the injection temperature might be partially responsible for the difference observed in the low-altitude and high-altitude scenarios. 60 Although the fraction of coating apparently did not change, cold temperature might already cause a partial collapse of the ramified structure, leading to smaller, already denser fresh soot particles.



65 **Figure S 1** Characterization of fresh soot before aging (absence of oxidants and light) during the various transport scenarios in AIDA: a) number size distribution; b) effective density and diameter relationship c) mass and diameter relationship; d) rBC mass fraction and diameter relationship. Soot produced with the mini-CAST burner (series 5200) operated with 60 μLPM of propane, 1.55 LPM of oxidation air, 7.5 LPM of N₂ and 13 LPM of dilution air. Scenarios: summer low-altitude (SL), winter low-altitude (WL), summer high-altitude (SH) and winter high-altitude (WH).

70

C. Mass concentration closure

75 By combining theDMA-APM-SP2 scans (Section 2.4.4 and Section 2.4.5) with the online and independent measurements performed by the SMPS and SP2 we performed a mass closure of the of the total aerosol mass present inside the AIDA chamber volume.

The M_{rBC} measured by the SP2 was converted into the mass concentration of the total aerosol (M_{P-SP2}) by means of the particle-by-particle coating mass fraction as:

80

$$M_{P-SP2} = M_{rBC} \left(1 + \frac{Fm_{coat}}{Fm_{rBC}} \right) \quad S1$$

Here we assumed that the particle-by-particle mass fraction of rBC and coating is representative of the rBC population, requiring a homogeneous coating degree across the SP2 detection size range.

- 85 The number size distribution of total particles measured by the SMPS was converted into a mass size distribution by accounting for the size-dependent effective density to determine the corresponding particle mass concentration (M_{P-SMPS}):

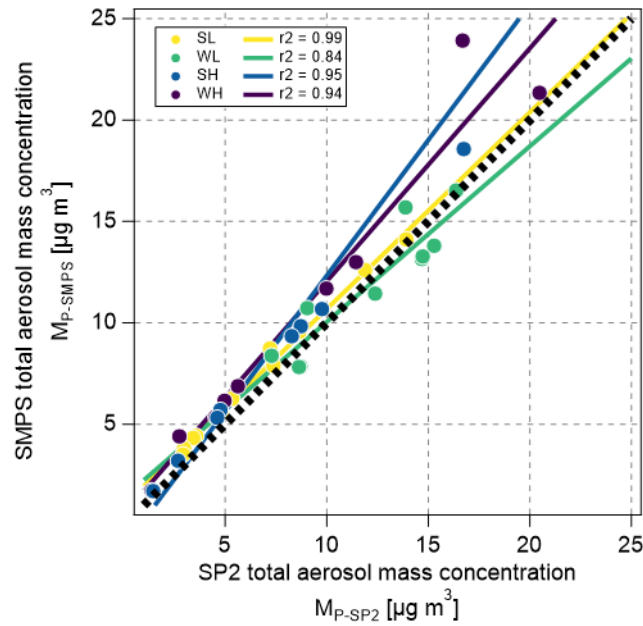
$$M_{P-SMPS} = \sum_{D_0}^{D_{max}} N_{Di-SMPS} * \rho_e(D_{i-SMPS}) * \frac{\pi D_{i-SMPS}^3}{6} \quad S2$$

- 90 where $\rho_e(D_{i-SMPS})$ is the effective density at a specific diameter of the SMPS size distribution (D_{i-SMPS}) and N_{i-SMPS} its number concentration.

$\rho_e(D_{i-SMPS})$ was extrapolated as a function of the mass-to-diameter relationship, which is described by an exponential function with the exponent (d_f) and constant (k_f) as follows:

$$\rho_e(D_{i-SMPS}) = \frac{6}{\pi} \frac{m_{Di-SMPS}}{D_{Di-SMPS}^3} = \frac{6}{\pi} \frac{(k_f * D_{i-SMPS})^{d_f}}{(D_{i-SMPS})^3} \quad S3$$

- 95 The M_{P-SP2} was compared with the M_{P-SMPS} to evaluate the accuracy of the independent measurement techniques, including DMA-APM, DMA-APM-SP2, SMPS, SP2, and AMS. This comparison also aimed to assess the validity of various assumptions, such as the material densities of BC, organic matter, and nitrate. The comparison was based on simultaneous measurements from the SP2 and SMPS, conducted one hour before and after each DMA-APM-SP2 scan.



100 **Figure S 2 Scatter plot with linear fitting between the total aerosol mass concentration derived from the SMPS and SP2.**

D. Characterization of diameter evolution

- 105 We investigated the temporal evolution of the geometric mean of the number size distribution of rBC ($D_{NrBC-GM}$) measured with the SP2, its growth factor (GF_{DrBC} , calculated as the ratio of D_{rBC-GM} at t_x to D_{rBC-GM} before t_0) and its growth rate (GR_{DrBC} , calculated as change of $D_{NrBC-GM}$ in a period Δt normalized over the period duration). The evolution of GF_{DrBC} and GR_{DrBC} is shown in Figure S3a. Since rBC

110 particles in the chamber are the refractory component and are assumed to be spherical in SP2 calculations,
changes in $D_{\text{NrBC-GM}}$ are attributed solely to intra-coagulation growth. Coagulation rates increases with
particle concentration (more collisions at higher concentrations) and the coagulation kernel, which varies
with particle diameter and diffusion coefficient (Naumann, 2003). In high-altitude experiments, fast
115 (50°N) and 85% by the experiment's end (90°N). In SL, lower rBC concentrations led to slower growth
($\text{GR}_{\text{DrBC}} \approx 1.5 \text{ nm h}^{-1}$), resulting in a 38% diameter increase within 24 hours (50°N) and 65% by the end
(90°N). Despite the different growth rate, diameter increased in these three experiments following an
exponential curve. GF_{DrBC} deviated from exponential growth in WL after the second aging step (t_{24}), when
120 GR_{DrBC} dropped to 0.1 nm h^{-1} while effective density, fractal dimension, and coating mass fraction
increased (50°N; Figure 5). This suggests that coating formation quickly compacted particles, reducing
coagulation rates (Naumann, 2003). Despite the higher concentration compared to SL, rBC particles
showed the slowest growth in WL, with final GF_{DrBC} below 60% (90°N). As discussed in Section 3.3, the
higher number and mass concentration in AIDA compared to ambient conditions might enhance
coagulation and diameter growth. However, it should be noted that rapid aging and the resulting
125 compaction may reduce coagulation rates near the sources (24 hours within emission) and in polluted
regions (below 50°N). While particle coagulation has been extensively studied in other settings (Schnaiter
et al., 2003; Maricq, 2007), the inhibition of growth by thick coating formation is a novel finding.

In a second analysis step, we investigated the temporal evolution of the geometric mean of the number
130 size distribution of total particles ($D_{\text{NP-GM}}$) measured with the SMPS, its growth factor (GF_{DP} , calculated
as the ratio of $D_{\text{NP-GM}}$ at t_x to $D_{\text{NP-GM}}$ before t_0) and its growth rate (GR_{DP} , calculated as change of $D_{\text{NP-GM}}$
in a period Δt normalized over the period duration). The evolution of GF_{DP} and GR_{DP} is shown in Figure
S3b.

Whereas coagulation increases diameter while maintaining external mixing (Naumann, 2003), coating
135 deposition first compacts and reduces size (Schnaiter et al., 2003; Yuan et al., 2020), then increases
diameter with coating thickening (Li et al., 2017). These processes occurred across different ARCTEx
scenarios. Exponential growth by coagulation was only observed during the coldest experiment (WH),
when no internal mixing was observed. The slight increase of ρ_e (Figure 5a) may have caused a deviation
from exponential growth in SL, when the slow GR_{DP} decreased at t_{24} , indicating a weaker coagulation
140 growth. Although rapid growth occurred in the first 24 hours (50°N) of SL, GF_{DP} decreased by 6% within
4 hours after the second aging step (t_{24}), indicating BC compaction similar to Schnaiter et al. (2003). The
steady increase in density and coating (Figure 5) caused the gradual collapse of BC 's ramified structure,
leading to a reduction in GF_{DP} from 61% at t_{24} to 53% at t_{72} and a negative GR_{DP} . After 70°N, as particles
approached spherical shapes, coating thickening drove growth, resulting in a final GF_{DP} of 80% (90°N).
145 Thin organic coatings ($\text{Fm}_{\text{coat}} \approx 0.20$) can compact fractal BC, reducing its mobility diameter (Bambha et
al., 2013). In WL, no exponential growth occurred. Rapid compaction likely took place in the very first
moment of the first aging step, followed by efficient nitrate deposition, which increased the coating
thickness of near-spherical particles in a stepwise manner, with growth rates exceeding 2 nm h^{-1} . Coating
growth appeared to be particularly efficient in the first 72 hours (70°N), when GF_{DP} reached 90% and
150 slowed afterwards. A similar step-wise growth was observed during medium-duration aging experiments
in AIDA (Schnaiter et al., 2005).

Overall, Figure S3b indicates that intra-coagulation may lead to faster growth then condensation and
coating formation. Nevertheless, even thin coatings may influence particle growth on short time scale
(WL and SL) and long-time scale (SH).

155

Scenarios: \blacksquare SL \square SH \bullet WL \circ WH
 AIDA operations: \square Light on \blacksquare Lights off ∇ Gas injection & T adjustment

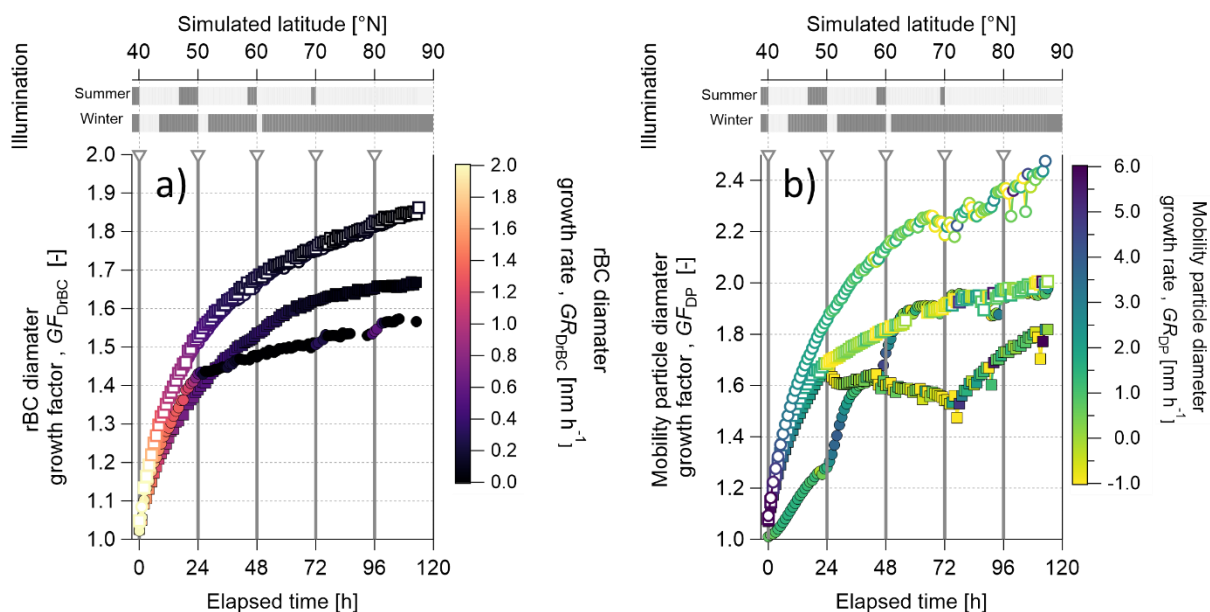


Figure S3 Temporal and latitudinal evolution of the growth factor and growth rate for: a) rBC particles measured with the SP2; b) total particles measured with the SMPS. ARCTEx scenarios: summer low-altitude (SL), winter low-altitude (WL), summer high-altitude (SH), winter high-altitude (WH).

160

E. References

- Bambha, R. P., Dansson, M. A., Schrader, P. E., and Michelsen, H. A.: Effects of volatile coatings and coating removal mechanisms on the morphology of graphitic soot, *Carbon*, 61, 80–96, <https://doi.org/10.1016/j.carbon.2013.04.070>, 2013.
- Cross, E. S., Onasch, T. B., Ahern, A., Wrobel, W., Slowik, J. G., Olfert, J., Lack, D. A., Massoli, P., Cappa, C. D., Schwarz, J. P., Spackman, J. R., Fahey, D. W., Sedlacek, A., Trimborn, A., Jayne, J. T., Freedman, A., Williams, L. R., Ng, N. L., Mazzoleni, C., Dubey, M., Brem, B., Kok, G., Subramanian, R., Freitag, S., Clarke, A., Thornhill, D., Marr, L. C., Kolb, C. E., Worsnop, D. R., and Davidovits, P.: Soot Particle Studies—Instrument Inter-Comparison—Project Overview, *Aerosol Sci. Technol.*, 44, 592–611, <https://doi.org/10.1080/02786826.2010.482113>, 2010.
- Ess, M. N., Bertò, M., Irwin, M., Modini, R. L., Gysel-Beer, M., and Vasilatou, K.: Optical and morphological properties of soot particles generated by the miniCAST 5201 BC generator, *Aerosol Sci. Technol.*, 55, 828–847, <https://doi.org/10.1080/02786826.2021.1901847>, 2021.
- Gysel, M., Laborde, M., Olfert, J. S., Subramanian, R., and Gröhn, A. J.: Effective density of Aquadag and fullerene soot black carbon reference materials used for SP2 calibration, *Atmospheric Meas. Tech.*, 4, 2851–2858, <https://doi.org/10.5194/amt-4-2851-2011>, 2011.
- Li, K., Chen, L., Han, K., Lv, B., Bao, K., Wu, X., Gao, X., and Cen, K.: Smog chamber study on aging of combustion soot in isoprene/SO₂/NO_x system: Changes of mass, size, effective density, morphology and mixing state, *Atmospheric Res.*, 184, 139–148, <https://doi.org/10.1016/j.atmosres.2016.10.011>, 2017.
- Liu, F., Snelling, D. R., Thomson, K. A., and Smallwood, G. J.: Estimate of scattering truncation in the cavity attenuated phase shift PMSSA monitor using radiative transfer theory, *Aerosol Sci. Technol.*, 52, 588–596, <https://doi.org/10.1080/02786826.2018.1437891>, 2018.
- Maricq, M. M.: Coagulation dynamics of fractal-like soot aggregates, *J. Aerosol Sci.*, 38, 141–156, <https://doi.org/10.1016/j.jaerosci.2006.11.004>, 2007.

185

- Maricq, M. M.: Examining the Relationship Between Black Carbon and Soot in Flames and Engine Exhaust, *Aerosol Sci. Technol.*, 48, 620–629, <https://doi.org/10.1080/02786826.2014.904961>, 2014.
- Moore, R. H., Ziemba, L. D., Dutcher, D., Beyersdorf, A. J., Chan, K., Crumeyrolle, S., Raymond, T. M., Thornhill, K. L., Winstead, E. L., and Anderson, B. E.: Mapping the Operation of the Miniature Combustion Aerosol Standard (Mini-CAST) Soot Generator, *Aerosol Sci. Technol.*, 48, 467–479, <https://doi.org/10.1080/02786826.2014.890694>, 2014.
- Naumann, K.-H.: COSIMA—a computer program simulating the dynamics of fractal aerosols, *J. Aerosol Sci.*, 34, 1371–1397, [https://doi.org/10.1016/S0021-8502\(03\)00367-7](https://doi.org/10.1016/S0021-8502(03)00367-7), 2003.
- Olfert, J. S., Symonds, J. P. R., and Collings, N.: The effective density and fractal dimension of particles emitted from a light-duty diesel vehicle with a diesel oxidation catalyst, *J. Aerosol Sci.*, 38, 69–82, <https://doi.org/10.1016/j.jaerosci.2006.10.002>, 2007.
- Pileci, R. E., Modini, R. L., Bertò, M., Yuan, J., Corbin, J. C., Marinoni, A., Henzing, B., Moerman, M. M., Putaud, J. P., Spindler, G., Wehner, B., Müller, T., Tuch, T., Trentini, A., Zanatta, M., Baltensperger, U., and Gysel-Beer, M.: Comparison of co-located refractory black carbon (rBC) and elemental carbon (EC) mass concentration measurements during field campaigns at several European sites, *Atmospheric Meas. Tech.*, 14, 1379–1403, <https://doi.org/10.5194/amt-14-1379-2021>, 2021.
- Rissler, J., Messing, M. E., Malik, A. I., Nilsson, P. T., Nordin, E. Z., Bohgard, M., Sanati, M., and Pagels, J. H.: Effective Density Characterization of Soot Agglomerates from Various Sources and Comparison to Aggregation Theory, *Aerosol Sci. Technol.*, 47, 792–805, <https://doi.org/10.1080/02786826.2013.791381>, 2013.
- Schnaiter, M., Horvath, H., Möhler, O., Naumann, K.-H., Saathoff, H., and Schöck, O. W.: UV-VIS-NIR spectral optical properties of soot and soot-containing aerosols, *J. Aerosol Sci.*, 34, 1421–1444, [https://doi.org/10.1016/S0021-8502\(03\)00361-6](https://doi.org/10.1016/S0021-8502(03)00361-6), 2003.
- Schnaiter, M., Linke, C., Möhler, O., Naumann, K.-H., Saathoff, H., Wagner, R., Schurath, U., and Wehner, B.: Absorption amplification of black carbon internally mixed with secondary organic aerosol, *J. Geophys. Res. Atmospheres*, 110, <https://doi.org/10.1029/2005JD006046>, 2005.
- Schnaiter, M., Gimmler, M., Llamas, I., Linke, C., Jäger, C., and Mutschke, H.: Strong spectral dependence of light absorption by organic carbon particles formed by propane combustion, *Atmospheric Chem. Phys.*, 6, 2981–2990, <https://doi.org/10.5194/acp-6-2981-2006>, 2006.
- Yon, J., Bescond, A., and Ouf, F.-X.: A simple semi-empirical model for effective density measurements of fractal aggregates, *J. Aerosol Sci.*, 87, 28–37, <https://doi.org/10.1016/j.jaerosci.2015.05.003>, 2015.
- Yuan, C., Zheng, J., Ma, Y., Jiang, Y., Li, Y., and Wang, Z.: Significant restructuring and light absorption enhancement of black carbon particles by ammonium nitrate coating, *Environ. Pollut.*, 262, 114172, <https://doi.org/10.1016/j.envpol.2020.114172>, 2020.